Bulletin of the Seismological Society of America, 90, 5, pp. 1305–1312, October 2000

Structure-Related and Stress-Induced Shear-Wave Velocity Anisotropy: Observations from Microearthquakes near the Calaveras Fault in Central California

by Jens C. Zinke and Mark D. Zoback

Abstract We attempt to distinguish between structure-related and stress-induced shear-wave velocity anisotropy in the upper crust using microearthquakes ($M \leq 2.6$) that occurred before and after the Tres Piños, California earthquake (M 5.5) of 26 January 1986. The Tres Piños earthquake occurred on the Quien Sabe fault, a northwest–southeast trending right-lateral strike-slip fault, approximately 10 km east of the Calaveras fault in central California. Digital, three-component seismograms are available from 1984 to 1992 from the Quien Sabe Ranch station (HQR), located only 7.3 km north-northeast of the epicenter of the main event.

We studied polarization directions and delay times using a method that combines cross-correlation techniques and particle-motion plots. To enhance the significance of our interpretations we reduced uncertainties related to the hypocenter-location of the earthquakes by source relocation based on joint-hypocenter determination and cross correlation.

In the study area we found two zones with different but stable polarization directions. Around the Quien Sabe fault system, shear-wave polarizations of over 30 microearthquakes clearly indicate that the slow shear-wave direction is normal to the northwest-southeast trend of this vertical right-lateral strike-slip fault. Thus, velocity anisotropy appears to be caused by the fault system itself. However, anisotropy associated with a cluster of microearthquakes located about 4 km to the east is quite different. In this zone the fast and slow shear-polarization directions are correlative with the maximum and minimum horizontal-stress directions, respectively. Thus in this case, it appears the crustal velocity anisotropy is controlled by the state of stress in the crust. The observation of these two polarization directions at one station suggests that the shallow crust below the station HQR does not influence shear-wave polarization directions.

Introduction

Shear-wave velocity anisotropy is caused by some form of effective anisotropy: differential stress anisotropy (e.g., stress-induced microcracks) or structural anisotropy (e.g., bulk anisotropy due to intrinsically anisotropic constituents, or bulk anisotropy due to the structure of isotropic constituents [e.g., plane thin layers]). Many recent papers address this problem in some form (e.g., Peacock *et al.,* 1988; Bernard and Zollo, 1989; Savage *et al.,* 1989; Zollo and Bernard, 1989; Aster *et al.,* 1990; Gledhill, 1991; Aster and Shearer, 1991, 1992; Zhang and Schwartz, 1994; Munson *et al.,* 1995; Bouin *et al.,* 1996; Coutant, 1996; Bernard *et al.,* 1997; Gamar and Bernard, 1997; Liu *et al.,* 1997).

The most popular explanation for shear-wave anisotropy is the hypothesis of "extensive dilatancy anisotropy" (EDA) that was suggested by Crampin (1978). This model assumes an isotropic crust where anisotropy is caused by the preferred orientation of vertical fluid-filled microcracks aligned in a direction controlled by the *in situ* stress field. This model has been modified since its introduction leading to the "anisotropic poroelasticity" model (APE) (Crampin and Zatsepin, 1997; Zatsepin and Crampin, 1997). However, many of the reported cases that use EDA to explain the observed shear-wave velocity anisotropy are ambiguous, because it is not possible to clearly differentiate among the different possible causes of anisotropy. For example, Bouin *et al.* (1996) studied the region around the Gulf of Corinth, Greece. This region is clearly being extended in the north–south direction. East–west trending normal faults are consistently parallel to the direction of maximum horizontal stress. The observed anisotropy was explained using EDA,

yet it could also have been explained by the structural anisotropy introduced by the consistent east–west orientation of the normal faults.

Moreover, results have been reported from several case studies where the EDA hypothesis did not seem applicable (e.g., Zollo and Bernard, 1989; Aster and Shearer, 1992; Zhang and Schwartz, 1994; Bernard *et al.*, 1997; Gamar and Bernard, 1997). Thus, it appears that the use of the EDA hypothesis needs a case by case evaluation, and there is a general need to improve our understanding of the causes of anisotropy.

To enhance our knowledge of the origin of crustal anisotropy, we found it favorable to study a region that is characterized by a maximum horizontal-stress direction that is not parallel to the trend of the main structural features. The South San Francisco Bay Area appears to be an appropriate region. Figure 1 illustrates the NW–SE trend of the major fault systems. Maximum horizontal-stress directions are shown for two extensively studied regions: the Morgan Hill segment of the Calaveras fault (Oppenheimer *et al.*, 1988) and the Loma Prieta segment of the San Andreas fault (Zoback and Beroza, 1993). These two regions are representative examples as they show maximum horizontal-stress directions that are almost perpendicular to the main structural features (reverse faults and fold axes).

Zhang and Schwartz (1994) studied shear-wave velocity anisotropy at the Loma Prieta segment of the San Andreas fault system and reported fast shear-wave polarizations that are predominantly fault-parallel. They suggested that the observed shear-wave velocity anisotropy could be produced by preferential mineral or microcrack alignment parallel to the dominant structural trends in the region, and the direction of shearing across the San Andreas fault. However, at one station that is farthest from the San Andreas fault, they observed fast shear-wave polarization directions that are parallel to the maximum horizontal stress in this region and consistent with the hypothesis of EDA. In our study, we decided to analyze shear-wave velocity anisotropy near the Quien Sabe Ranch station (HQR), which is located about 15 km east of the Calaveras fault immediately to the south of the region shown in Figure 1.

There has been a lot of controversy about temporal changes of seismic anisotropy (e.g., Peacock *et al.*, 1988; Savage *et al.*, 1989; Aster *et al.*, 1990; Munson *et al.*, 1995; Bernard *et al.*, 1997; Gamar and Bernard, 1997; Liu *et al.*, 1997). Unfortunately, when sampled in time, the data we consider here are too sparse to be used to study temporal variations of seismic anisotropy such that this topic is thus not considered in this article.

Data Set and Data Analysis

Our study area has the advantage that the epicenter of the Tres Piños, California, earthquake (M 5.5) of 26 January 1986 is located at the Quien Sabe fault system (QS) that is only 7.3 km SW of the station HQR (Fig. 2). QS is a right-lateral strike-slip fault system that trends NW–SE. Microearthquakes occurred before and after the main event. Digital, three-component seismograms with a sampling rate of 100 samples per second are available for events that occurred from 1984 to 1992.

In Figure 2, microearthquake ($M \leq 2.6$) epicenter locations reveal the Tres Piños fault system (TP), the Quien Sabe fault system (QS), and a swarm of microearthquakes close to the Cibo Peak (CP). The depth of the earthquake occurrence is shown in a section along line AA′ using perpendicular projection (Fig. 3). It appears that the fault systems are almost vertical.

The analysis of shear-wave polarization requires that incident angles be less than the critical angle ($i_c = \sin^{-1}(v_S/v_P)$, where v_P and v_S are the surface velocities of the P and S waves, respectively) to avoid contamination of the first arriving shear wave by the converted S to P wave on the free surface (Nuttli, 1961). The reflected P wave causes elliptical particle motion that may be misinterpreted. Therefore, we used only those earthquakes that are within the shear-wave window (i.e., those earthquakes that are within the cone delineated by the critical angle). No earthquakes from TP, only some earthquakes from QS, and all of the earthquakes from CP have been used.

We started our analysis with the selection of appropriate records. The shear-wave critical angle is about 35° for a plane wave incident on the free surface of a homogeneous half-space with a Poisson's ratio of 0.25 (Nuttli, 1961). However, we examined all of those earthquakes from the Northern California Seismic Network (NCSN) database that have a theoretical incident angle of 45°, since the effect of a low-velocity shallow layer significantly increases the shear-wave window (Bernard and Zollo, 1989). The theoretical incident angle was deducted from the source location, and we checked that the observed incidence angle of the P wave was smaller than 35°. Then, we bandpass-filtered the recorded seismograms in the range of 1.25 and 12.50 Hz and excluded seismograms from further observations that had a signal-to-noise ratio of less than 3.

Shear-wave velocity anisotropy is revealed by the arrival of two split shear waves that are separated in time. We use delay time to refer to the time difference between the arrival of the fast and slow shear waves. The delay time depends on the degree of anisotropy and the length of the wave path through the anisotropic medium. Furthermore, we characterize the anisotropy of the medium by polarization directions that are obtained for the fast and slow shear waves. To choose the best method for our analysis, we tested different methods that have been described elsewhere, for example, visual inspection of particle motion plots, covariance matrix decomposition, and cross-correlation (e.g., Zhang and Schwartz, 1994). Covariance matrix decomposition is widely used (e.g., Jurkevics, 1988; Aster *et al.*, 1990; Zhang and Schwartz, 1994), but it requires subjective criteria to define the arrival of the fast shear wave (i.e., the

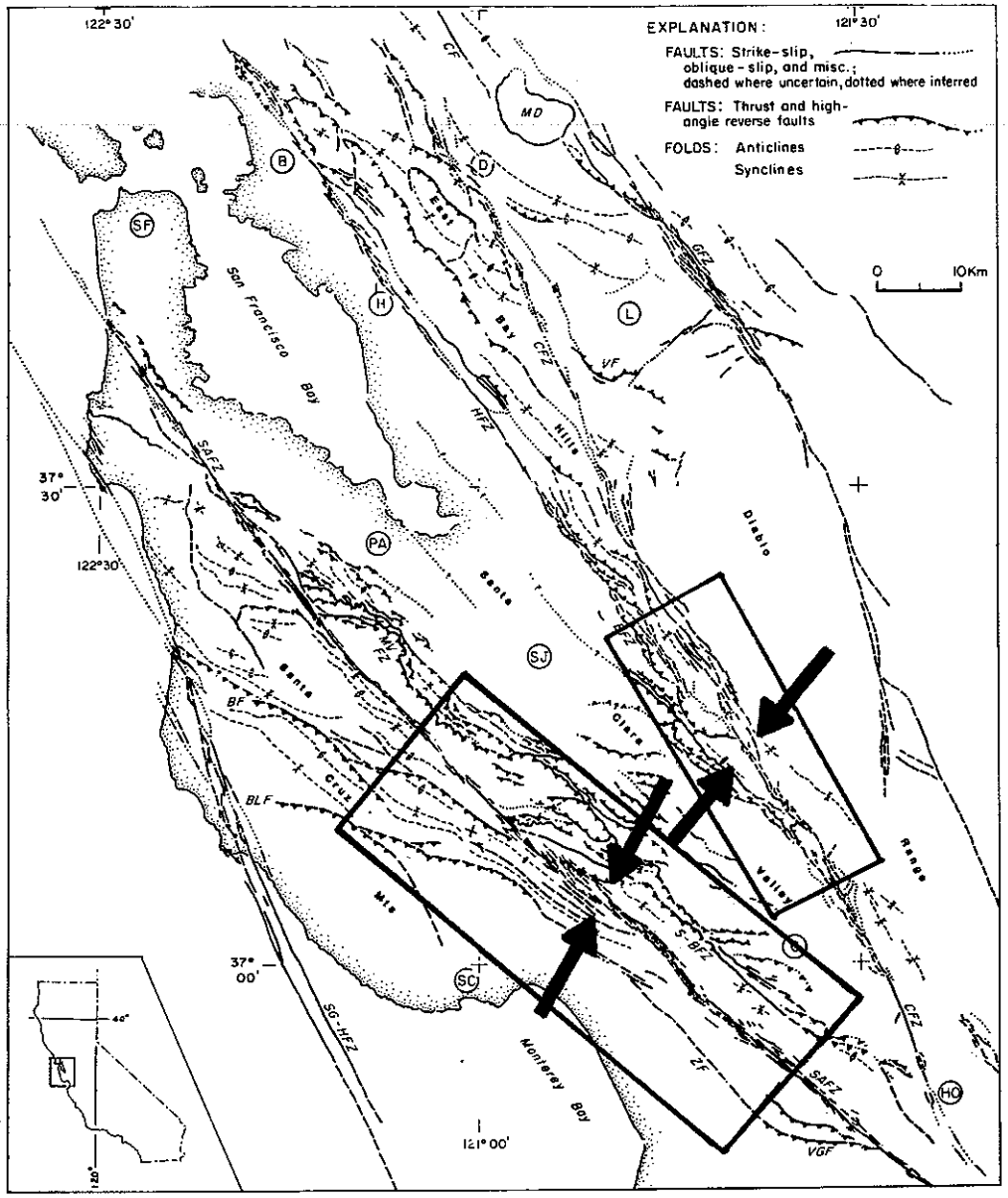

Figure 1. Map of Pliocene-Quaternary structures, San Francisco Bay Area (modified after Aydin and Page, 1984). Maximum horizontal-stress directions observed for the region of the Morgan Hill segment of the Calaveras fault (upper box, Oppenheimer *et al.*, 1988), and the region of the Loma Prieta segment of the San Andreas fault (lower box, Zoback and Beroza, 1993). Note that the observed stress directions are nearly perpendicular to the strike of the faults. B, Berkeley; BF, Butano fault; BLF, Ben Lomond fault; CF, Concord fault; CFZ, Calaveras fault zone; D, Danville; EFZ, Evergreen fault zone; G, Gilroy; GFZ, Greenville fault zone; H, Hayward; HFZ, Hayward fault zone; HO, Hollister; L, Livermore; MD, Mount Diablo; MVFZ, Monte Vista fault zone; PA, Palo Alto; SAFZ, San Andreas fault zone; S-BFZ, Sargent-Berrocal fault zone; SC, Santa Cruz; SF, San Francisco; SG-HFZ, San Gregorio-Hosgri fault zone; SJ, San Jose; VF, Verona fault; VGF, Vergeles fault; ZF, Zayante fault.

start of linear motion). Interpretation errors rise with decreasing initial linear motion (i.e., for decreasing delay time) and/or decreasing signal-to-noise ratio. We found that the least biased results are obtained if a method is used that is based on cross-correlation techniques and particle motion plots (see appendix). Using cross-correlation techniques, we assume that one homogeneous anisotropic layer is the only source of perturbation to the shear wave. This is a constraining but reasonable hypothesis, as it is suggested by the simple and clear seismograms of our data set (see Fig. A1).

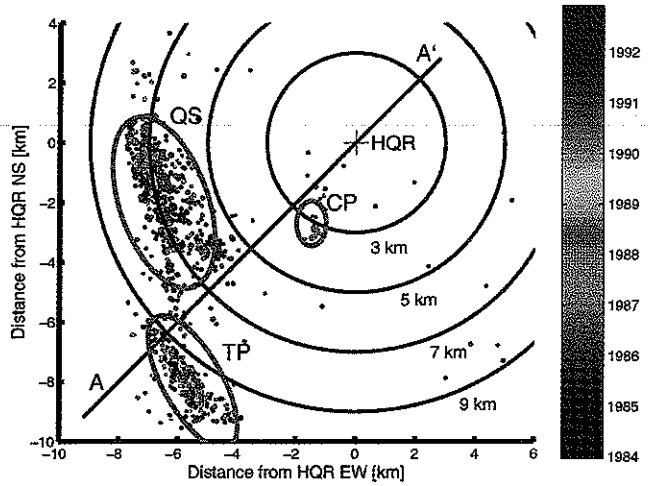

Figure 2. Map of the vicinity of the Quien Sabe Ranch station (HQR). Epicenter location of microearthquakes reveal the Tres Piños fault system (TP), the Quien Sabe fault system (QS), and a swarm of microearthquakes close to the Cibo Peak (CP). The time of occurrence of the earthquakes is shown by the color of the symbols. Horizontal distance from HQR is denoted by circles. The depth of the earthquake location is shown in a section along line AA′ using perpendicular projection (see Fig. 3).

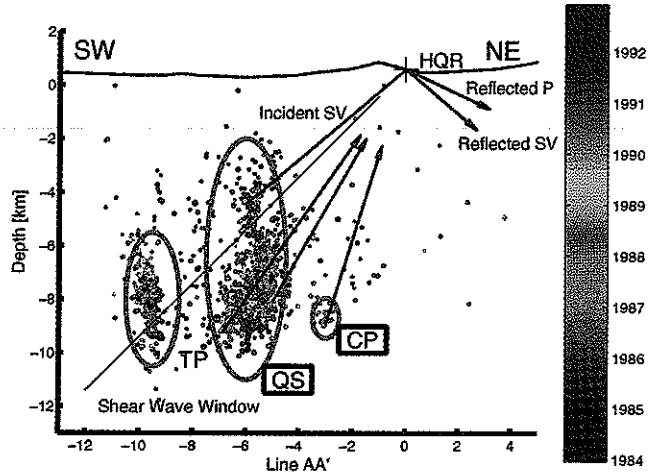

Figure 3. Earthquakes from Figure 2 are shown in a section along line AA′ using perpendicular projection. The location of the events reveals that TP and QS are almost vertical fault zones. Wave paths are shown for different events. Events with an incident angle that is larger than the critical value (e.g., Nuttli, 1961) will show converted *S* to *P* waves (reflected *P* wave). These events are outside the shear-wave window and have not been used in this study. Note that the wave paths of the events that can potentially be used are merging in the shallow crust below the station HQR. The actual wave paths will be even closer if a low velocity layer is present in the shallow crust.

Results and Discussion: Polarization Directions and Delay Times

Our main results are summarized in the map in Figure 4. The analyzed microearthquakes are shown by symbols that are assigned to the epicenter. The tail of the symbols shows in direction (horizontal projection) of the first motion of the fast shear wave. The length of the tail is proportional to the delay time.

We distinguish between two major zones: (1) the zone of QS, and (2) the zone close to CP. Those zones are characterized by significant delay times and stable but different polarization directions.

For microearthquakes that occurred at QS, fast shear waves are polarized in a NW–SE direction. Observed delay times vary between 0.04 and 0.21 sec with a mean of 0.07 sec and a standard deviation of 0.05 sec. For microearthquakes that occurred at CP, fast shear waves are polarized in NNE–SSW direction. Delay times vary between 0.04 and 0.12 sec with a mean of 0.06 sec and a standard deviation of 0.03 sec.

Since the observed shear-wave polarization directions could be caused by source effects, we compared predicted and observed polarization directions of 34 earthquakes (Fig. 5).

The predicted polarization directions have been obtained from radiation patterns (Aki and Richards, 1980) using fault plane mechanisms from the NCSN database that have been obtained from *P*-wave first motions. Errors in the fault plane solutions may cause errors in the derived radia-

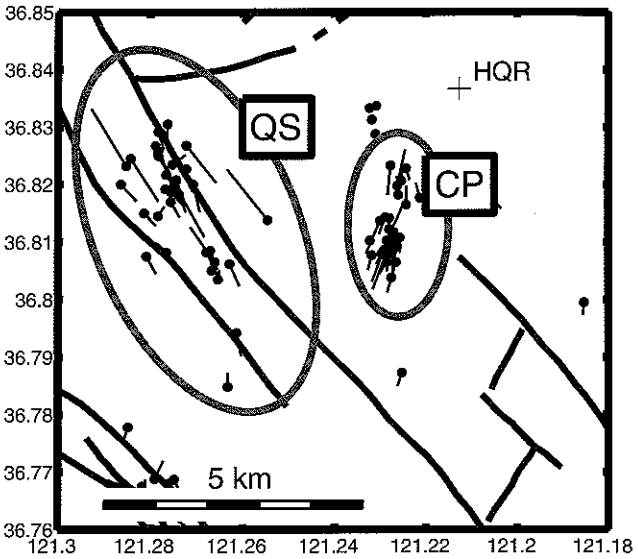

Figure 4. Map of the vicinity of the station HQR. Previously mapped faults are shown in red (Robbins, 1982). Symbols are assigned to the epicenter of the studied earthquakes. The tail of the symbol shows in direction of the first motion of the first arriving shear wave. The length of the symbol is proportional to the delay time. Two zones with stable polarization directions and significant delay times are marked (QS and CP).

tion patterns. However, these errors are expected to be small, since polarization directions vary slowly over the focal sphere (except for observations along the two lines that connect the *P*- and *T*-axes and the intersection of the fault and nodal planes). Analyzing the results presented in Figure 6 in detail, we acknowledge that the observed first shear-polarization vector and the predicted polarization vector make an angle of more than 90° for many of the observed microearthquakes. This is not compatible with the splitting of the predicted shear wave into a first shear wave in the observed directions. We found the explanation in strike-slip events that are radiated from QS and arrive at the station HQR at an angle that is likely to cause large errors in the predicted shear wave polarization (see the earlier statement about errors). This may appear to weaken our arguments. However, (1) significant differences between radiated and observed polarization directions, (2) events with different source mechanisms, and (3) the fact that the observed polarization directions are stable for both QS and CP indicate that shear-wave polarization is caused by effective anisotropy and not by source effects. In an isotropic crust, the observed shear-wave polarizations would have been those radiated from the source modified only due to interactions with the free surface and interfaces along the ray path. In an anisotropic crust, however, the radiated polarization is split into two shear waves, unless the polarization direction is exactly parallel with one of the principal directions of anisotropy. The faster of the two split shear waves is observed as a first-arriving shear wave.

Two facts suggest that the upper layer of the crust below the station does not influence shear-wave polarization directions: (1) the observed shear-wave polarization directions are different for QS and CP, and (2) they are caused by effective anisotropy. A study by Aster and Shearer (1991) addresses the anisotropy of the highly weathered upper 300 m of the crust. It indicates that this zone can be isotropic. However, an isotropic upper layer appears to contradict results reported by many other researchers (e.g., Gledhill, 1991; Zhang and Schwartz, 1994; Munson *et al.*, 1995; Coutant, 1996), who found that seismic anisotropy is ubiquitous in the shallow crust. In our study area, rock formations are composed of mainly sandstone. These rock formations do not suggest intrinsic anisotropy. However, the upper layer is known to be composed of the most altered rock formations, and fractures are usually assumed to be the cause of anisotropy. In this case, we would expect one single polarization direction if the waves have essentially the same path. The fact is that the events from QS and CP have merging wave paths in the

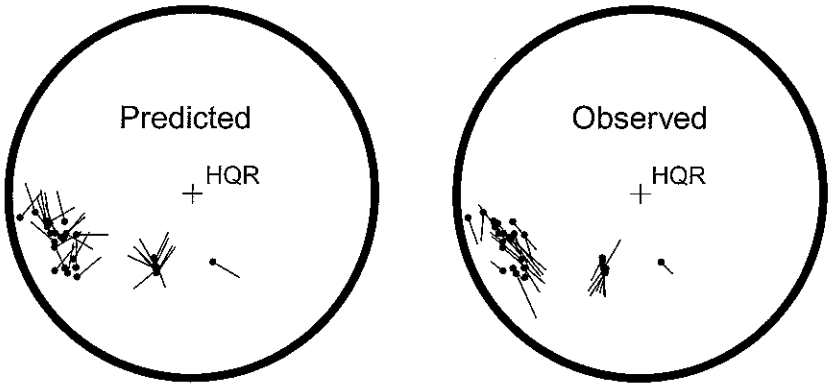

Figure 5. Predicted (from radiation pattern) and observed polarization directions of the first arriving shear wave. The diagrams are equal-area projections. The radius corresponds to an incident angle of 45°. Symbols are assigned to the hypocenter location. The tail of the symbols shows in direction of the first motion of the leading shear wave.

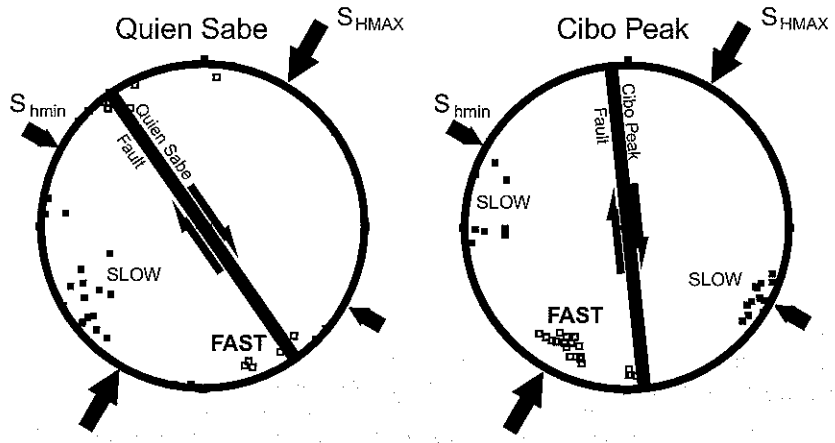

Figure 6. Principal horizontal-stress directions (arrows), fault plane orientations, and shear-wave polarization directions (open squares, fast shear wave polarization; filled squares, slow shear wave) are shown in equal-area projections for the QS zone and for the CP zone.

upper low-velocity layer below the station, yet show different polarization directions (see Fig. 3).

To answer the question about the causes of anisotropy for both, QS and CP, we compared (1) directions of the principal horizontal stresses, (2) fault plan orientations, and (3) shear-wave polarization directions. Our results are summarized in equal area plots (see Figure 6).

Principal horizontal-stress directions have been obtained from focal-plane mechanism data of the NCSN database using analysis routines for inversion (Gephart, 1990; Gephart and Forsyth, 1984). The obtained results are consistent with other observations (e.g., Zoback *et al.,* 1987; Oppenheimer *et al.,* 1988; Zoback and Beroza, 1993). The orientation of the fault planes have been obtained for QS as an average of the direction of the segments of the mapped Quien Sabe fault system (Robbins, 1982), and for CP from relative locations of earthquake hypocenters (Fig. 7). Fast and slow shear-wave polarization directions are obtained using the algorithm described in the appendix.

For QS, the polarization directions of the slow shear wave are normal to the northwest–southeast trend of the vertical right-lateral strike-slip fault system, and the polarization directions of the fast shear wave are not correlative with the maximum horizontal-stress direction (S_{HMAX}). Thus, the observed shear-wave polarization directions appear to be caused by the fault zone itself.

For CP, the fast and slow shear-wave polarization directions are close to the orientation of the maximum (S_{HMAX}) and minimum (S_{hmin}) horizontal stress, respectively. The Cibo Peak fault is clearly not oriented with respect to the shear-wave polarization directions. Note the difference of almost 30°. Thus, the observed shear-wave polarization directions appear to be consistent with being controlled by the state of stress in the crust. Vertical fluid-filled cracks and fractures that are opened with respect to the maximum horizontal stress (EDA cracks) but not the orientation of the fault are a possible explanation.

The orientation of the Cibo Peak fault has been obtained using fault plane solutions from the NCSN database (see Fig. 7).

The results have been confirmed by determining the relative location of the earthquake hypocenters using joint-hypocenter determination and cross-correlation (Ellsworth, 1977; Roecker, 1981; Dodge *et al.,* 1995). Absolute hypocenter locations of the NCSN database had not been used for this analysis because of large location errors. Results shown in Figure 6 also reveal that the angle between the strike of Quien Sabe fault and the orientation of S_{HMAX} (~65°) is much bigger than the angle between the strike of Cibo Peak fault and the orientation of S_{HMAX} (~30°). According to Zoback *et al.* (1987), frictional faulting theory suggests that the Quien Sabe fault must be a "weak fault," whereas the Cibo Peak fault appears to be a "strong fault." Thus, it appears that factors such as high pore pressure or aligned weak minerals that may cause the Quien Sabe fault to be "weak" are also possible causes of the observed shear-wave velocity anisotropy.

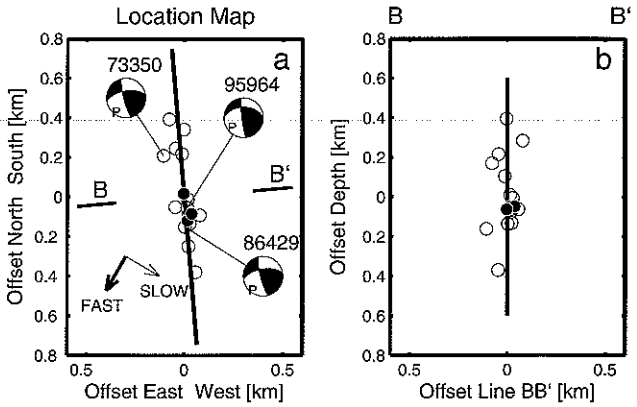

Figure 7. Relative locations of the microearthquakes that occurred close to the Clbo Peak are shown in map view and in a section along line BB′ (perpendicular projection). Relative locations have been obtained using joint-hypocenter determination and cross-correlation techniques (Ellsworth, 1977; Roecker, 1981; Dodge *et al.,* 1995).

Conclusions

Our observations lead us to the following conclusions:

1. The upper layer of the crust (upper 2 to 4 km) appears to be isotropic in the studied area, as two different but stable polarization directions have been observed at one station.
2. Velocity anisotropy, observed around the Quien Sabe fault system, appears to be caused by the fault system itself. Shear-wave polarization of over 30 microearthquakes clearly indicates that the direction of the slow shear-wave polarization is normal to the NW–SE trend of this vertical right-lateral strike-slip fault system. Moreover, the fault system appears to be "weak," as the angle between the strike of this fault system and the maximum horizontal compression exceeds the angle of 30° to 45° that would be predicted from frictional faulting theory. High pore pressure or the alignment of weak minerals are assumed to be causes of near-frictionless faulting and may also be an explanation for the observed shear-wave velocity anisotropy.
3. Velocity anisotropy associated with a cluster of microearthquakes located only 4 km to the east of the Quien Sabe fault system appears to be controlled by the state of stress in the crust. In this zone the fast and slow shear directions are correlative with the maximum and minimum horizontal stress directions, respectively.

Acknowledgments

This study has been carried out at Stanford University. We used data from the Northern California Seismic Network (NCSN) and wish to thank everyone who maintains this network and the database. We wish to thank David Schaff for processing data to determine relative locations of the earthquake hypocenters. We also thank Rick Aster and two anonymous reviewers who contributed with suggestions and comments. Jens Zinke is supported by the Deutsche Forschungsgemeinschaft (Grant Zi 559-1/1) and by the Blaustein Foundation.

References

Aki, K., and P. G. Richards (1980). *Quantitative Seismology, Theory and Methods,* Vol. 1, W. H. Freeman, San Francisco, 557 pp.

Aster, R. C., P. M. Shearer, and J. Berger (1990). Quantitative measurements of shear wave polarizations at the Anza Seismic Network, Southern California: implications for shear wave splitting and earthquake prediction, *J. Geophys. Res.* **95,** 12449–12473.

Aster, R. C., and P. M. Shearer (1991). High-frequency borehole seismograms recorded in the San Jacinto Fault Zone, Southern California. Part 1. Polarizations, *Bull. Seism. Soc. Am.* **81,** 1057–1080.

Aster, R. C., and P. M. Shearer (1992). Initial shear wave particle motions and stress constraints at the Anza Seismic Network, *Geophys. J. Int.* **108,** 740–748.

Aydin, A., and R. M. Page (1984). Diverse Pliocene-Quarternary tectonics in a transform environment, San Francisco Bay region, California, *Geol. Soc. Am. Bull.* **95,** 1303–1317.

Bernard, P., and A. Zollo (1989). Inversion of near-source polarization of parameters of double-couple point like sources, *Bull. Seism. Soc. Am.* **79,** 1779–1809.

Bernard, P., G. Chouliaras, A. Tzanis, P. Briole, M.-P. Bouin, J. Tellez, G. Stavrakakis, and K. Makropoulos (1997). Seismic and electrical anisotropy in the Mornos delta, Gulf of Corinth, Greece, and its relationship with GPS strain measurements, *Geophys. Res. Lett.* **24,** 2227–2230.

Bouin, M.-P., J. Téllez, and P. Bernard (1996). Seismic anisotropy around the Gulf of Corinth, Greece, deduced from three-component seismograms of local earthquakes and its relationship with crustal strain, *J. Geophys. Res.* **101,** 5797–5811.

Coutant, O. (1996). Observations of shallow anisotropy on local recordings at the Garner Valley, Southern California, downhole array, *Bull. Seism. Soc. Am.* **86,** 477–488.

Crampin, S. (1978). Seismic-wave propagation through a cracked solid: polarization as a possible dilatancy diagnostic, *Geophys. J. R. Astr. Soc.* **53,** 467–496.

Crampin, S., and S. V. Zatsepin (1997). Modeling the compliance of crustal rock—II. Response to temporal changes before earthquakes, *Geophys. J. Int.* **129,** 495–506.

Dodge, D. A., G. C. Beroza, and W. L. Ellsworth (1995). Foreshock sequence of the 1992 Landers earthquake and its implications for earthquake nucleation, *J. Geophys. Res.* **100,** 9865–9880.

Ellsworth, W. L. (1977). Three-dimensional structure for the crust and mantle beneath the island of Hawaii, *Ph.D. Thesis,* Massachusetts Institute of Technology, Cambridge, 327 pp.

Gamar, F., and P. Bernard (1997). Shear wave anisotropy in the Erzincan basin and its relationship with crustal strain, *J. Geophys. Res.* **102,** 20373–20393.

Gephart, J. W. (1990). Stress and the direction of slip on fault planes, *Tectonics* **9,** 845–858.

Gephart, J. W., and D. W. Forsyth (1984). An improved method for determining the regional stress tensor using earthquake focal mechanism data: application to the San Fernando sequence, *J. Geophys. Res.* **89,** 9305–9320.

Gledhill, K. R. (1991). Evidence for shallow and pervasive seismic anisotropy in the Wellington region, New Zealand, *J. Geophys. Res.* **96,** 21503–21516.

Jurkevics, A. (1988). Polarization analysis of three-component array data, *Bull. Seism. Soc. Am.* **78,** 1725–1743.

Liu, Y., S. Crampin, and I. Main (1997). Shear-wave anisotropy: spatial and temporal variations in time delays at Parkfield, Central California; *Geophys. J. Int.* **130,** 771–785.

Munson, C. G., C. H. Thurber, Y. Li, and P. G. Okubo (1995). Crustal shear wave anisotropy in southern Hawaii: spatial and temporal analysis, *J. Geophys. Res.* **100,** 20367–20377.

Nuttli, O. (1961). The effect of the Earth's surface on the *S* wave particle motion, *Bull. Seism. Soc. Am.* **44,** 237–246.

Oppenheimer, D. H., P. A. Reasenberg, and R. W. Simpson (1988). Fault plane solutions for the 1984 Morgan Hill, California, earthquake sequence: evidence for the state of stress on the Calaveras fault, *J. Geophys. Res.* **93,** 9007–9026.

Peacock, S., S. Crampin, and D. C. Booth (1988). Shear wave splitting in the Anza seismic gap, southern California: temporal variations as possible precursors, *J. Geophys. Res.* **93,** 3339–3356.

Robbins, S. L. (1982). Complete Bouguer gravity, aeromagnetic, and generalized geologic map of the Hollister 15-minute quadrangle, California, Geophysical Investigations Map, U.S. Geological Survey.

Roecker, S. W. (1981). Seismicity and tectonics of the Pamir-Hindu Kush region of central Asia, *Ph.D. Thesis,* Massachusetts Institute of Technology, Cambridge, 294 pp.

Savage, M. K., X. R. Shih, R. P. Meyer, and R. C. Aster (1989). Shear-wave anisotropy of active tectonic regions via automated *S*-wave polarization analysis, *Tectonophysics* **165,** 279–292.

Zatsepin, S. V., and S. Crampin (1997). Modeling the compliance of crustal rock—I. Response of shear wave splitting to differential stress, *Geophys. J. Int.* **129,** 477–494.

Zhang, Z., and S. Y. Schwartz (1994). Seismic anisotropy in the shallow crust of the Loma Prieta segment of the San Andreas fault system, *J. Geophys. Res.* **99,** 9651–9661.

Zoback, M. D., M. L. Zoback, V. S. Mount, J. Suppe, J. P. Eaton, J. H. Healy, D. Oppenheimer, P. Reasenberger, L. Jones, C. B. Raleigh, I. G. Wong, O. Scotti, and C. Wentworth (1987). New evidence on the state of stress of the San Andreas fault system, *Science* **238,** 1105–1111.

Zoback, M. D., and G. C. Beroza (1993). Evidence for near-frictionless faulting in the 1989 (*M* 6.9) Loma Prieta, California, earthquake and its aftershocks, *Geology* **21,** 181–185.

Zollo, A., and P. Bernard (1989). *S*-wave polarization inversion of the 15 October 1979, 23:19 Imperial Valley aftershock: evidence for anisotropy and a simple source mechanism, *Geophys. Res. Lett.* **16,** 1047–1050.

Appendix

Shear-Wave Polarization and Delay-Time Analysis

We estimated polarization directions and delay time using a method that is based on cross-correlation techniques and particle-motion plots. An example is given for event 73350 (NCSN-catalog) shown in Figure A1.

Particle-motion plots in Figure A2 (a1–a3) show elliptical particle motion consistent with shear-wave splitting. The shear waves are polarized in a plane different from the horizontal plane. To obtain the polarization directions we rotated the coordinate system iteratively. Each step comprised decomposition of the particle motion into three perpendicular seismograms and cross-correlation of them by shifting one seismogram along the time axis. A new coordinate system with axes aligned parallel to the two split shear-wave polarization directions is obtained corresponding to the highest value of the cross-correlation coefficient. Particle-motion plots for the new coordinate system are shown in Figure A2 (b1–b3).

We confirmed the results that were automatically obtained by visual comparison of the fast (nN) and the slow (nE) shear waves (Fig. A3). We require that (1) both shear waves are clearly identifiable and similar, and (2) particle motion be negligible in the direction normal to the shear-wave polarization plane (nZ).

The delay time is obtained as a result of the cross correlation from the time shift between fast and slow shear

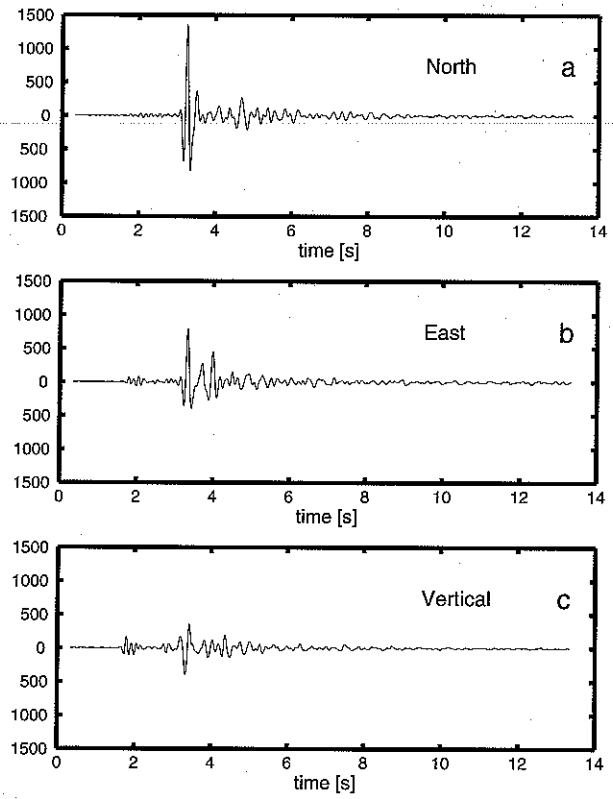

Figure A1. Seismograms of event 73350 (NCSN catalog) are shown in the recorded directions.

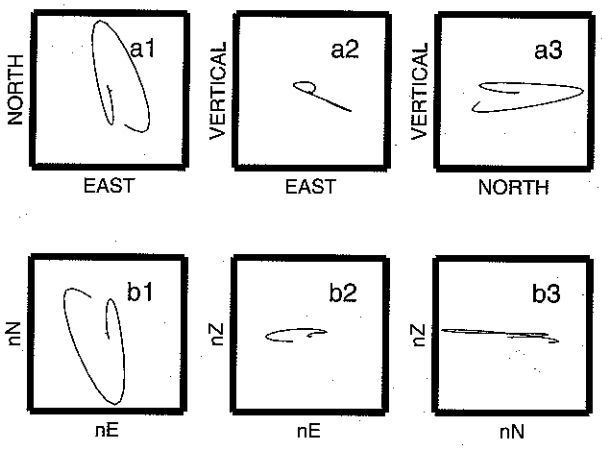

Figure A2. Particle-motion plots of the shear wave are shown in two different coordinate systems: (a1–a3) geographical coordinate system and (b1–b3) coordinate system corresponding to the polarization directions. The time interval is 40 msec.

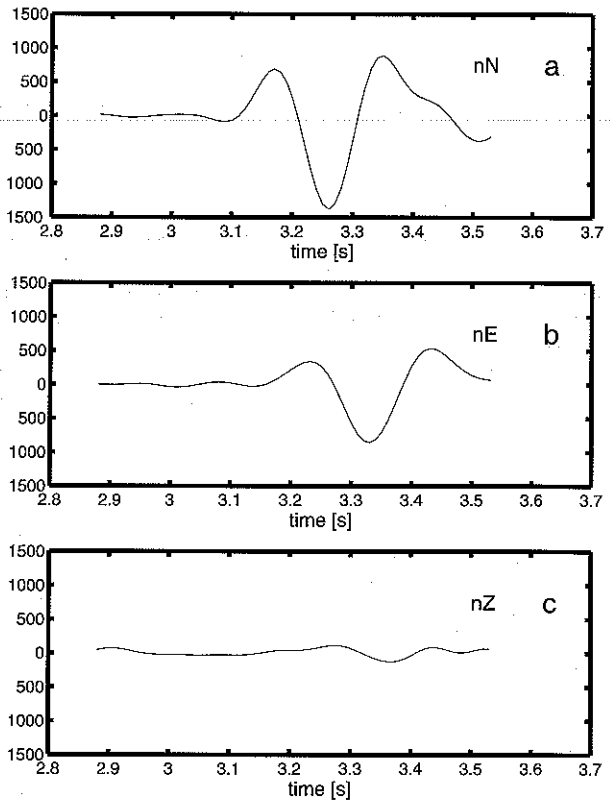

Figure A3. Seismograms of the shear wave are shown in a coordinate system that corresponds to the polarization directions. Fast (a) and slow (b) shear waves are similar. The delay time is about 0.07 sec. The signal in the direction perpendicular to the shear wave polarization plane (c) is negligible.

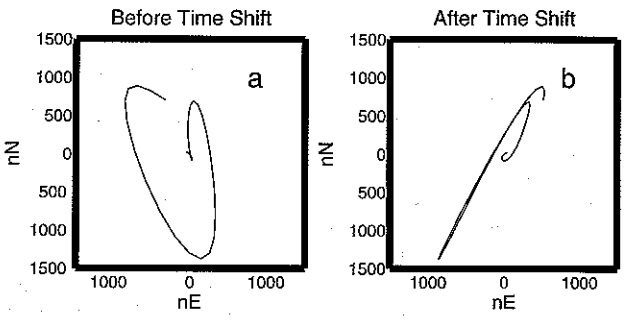

Figure A4. Particle-motion plot for shear waves before (a) and after (b) a time shift of the slow shear wave for 0.07 sec.

waves. This result is confirmed by examining particle-motion plots that are produced before and after shifting the slow shear wave along the time axis (Fig. A4). Ideally, we expect to obtain a line in a particle-motion plot, if the wave forms are similar, and delay time and polarization directions are determined correctly.

Stanford University
Department of Geophysics, Mitchell Building B55
Stanford, California 94305
Zinke@pangea.stanford.edu

Manuscript received 9 July 1999.